Nano Research

Open Access

Research Article

Interfacial modification strategy by lead chloride post-treatment enables 8.05% efficient Sb_2S_3 solar cells

Guohuan Shen[1,§], Ruiheng Gao[1,§], Shiwu Chen[1], An Ke[1], Tianjun Ma[1], Salman Ali[1], Mingyu Li[1], Hsien-Yi Hsu[2], Jiang Tang[1], and Haisheng Song[1] ✉

[1] *Wuhan National Laboratory for Optoelectronics and School of Optical and Electronic Information, Huazhong University of Science and Technology, Wuhan 430074, China*
[2] *School of Energy and Environment & Department of Materials Science and Engineering, City University of Hong Kong, Kowloon Tong, Hong Kong 999077, China*
[§] *Guohuan Shen and Ruiheng Gao contributed equally to this work.*

Cite this article: *Nano Research*, **2025**, *18*, 94908031. https://doi.org/10.26599/NR.2025.94908031

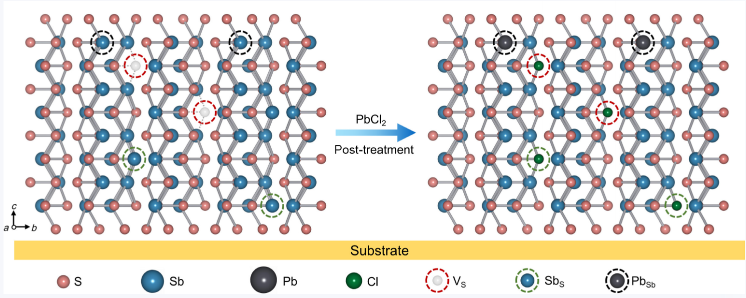

ABSTRACT: Antimony sulfide (Sb_2S_3) is a competitive photovoltaic material, especially for tandem solar cells. However, the quasi-intrinsic carrier concentration and deep work function of Sb_2S_3 cause serious extraction problem at Sb_2S_3/hole-transport-layer (HTL) interface. In this study, we proposed an efficient strategy to modify the Sb_2S_3/HTL interface by lead chloride ($PbCl_2$) post-treatment. Our results demonstrated that Cl incorporation could passivate the defect of sulfur vacancy (V_S) and antisite (Sb_S), and Pb enabled effective p-type doping at the Sb_2S_3 interface with the Cl help of V_S removal. The synergistic effect of Pb and Cl elements matched well with HTL energy level, facilitated hole extraction and enhanced the interface conductivity. By employing $PbCl_2$ treatment, the resulting devices obtained a high fill factor (FF) of 66.02%, and a top power conversion efficiency (PCE) of 8.05%. This work provides valuable insights into improving the Sb_2S_3 interface for enhancing solar cell performance.

KEYWORDS: antimony sulfide, solar cells, interfacial modification, hole extraction

1 Introduction

Antimony chalcogenides (Sb_2X_3, X = S, Se) have garnered significant attention in recent years, particularly Sb_2S_3, which is considered as one of the ideal top-cell materials for tandem solar cells. Besides wide-bandgap (WBG) Sb_2S_3, the performance of WBG inorganic perovskite solar cells have obtained fast development in recent years [1]. It is pity that they still face challenges such as stability [2], toxicity, sensitive interface [3] etc. and need more research effort to meet the commercial application. Sb_2S_3 has advantages such as high absorption coefficient, environmental friendliness, stability, and suitable bandgap of approximately 1.7 eV [4, 5]. Despite these advantages, the highest reported certified power conversion efficiency of Sb_2S_3 solar cells remains at 8.08% [6], much room below its theoretical efficiency limit of 28.64%. Recent research efforts have predominantly focused on enhancing the quality of the Sb_2S_3 absorber layer [7, 8]. However, the interface between the Sb_2S_3 absorber and the transport layer also plays a critical role in device performance [9, 10].

The interface between the electron transport layer (ETL) and the absorption layer has been extensively studied in antimony chalcogenides solar cells in recent years [11–16]. Due to the complex defects in Sb_2S_3, including sulfur vacancy (V_S) and antisite (Sb_S) defects, its quasi-intrinsic character and deep work function easily induced high back contact barrier at the interface of Sb_2S_3/hole transport layer (HTL) [17–20]. In 2014, Seok's group introduced a post-treatment process using thioacetamide (TA) for Sb_2S_3, which released H_2S to reduce oxide content and deep defects in the film. This approach achieved a milestone power conversion efficiency (PCE) of 7.5% [21]. Postsurface selenization and tellurization were adopted to suppress the rear contact barrier to improve the fill factor and carrier extraction capability [22, 23]. Xiao et al. developed a simplified strategy to improve the

---

Received: June 30, 2025; **Revised:** August 31, 2025
Accepted: September 2, 2025

✉Address correspondence to songhs-wnlo@mail.hust.edu.cn

morphology and crystallinity of thin films via an alkali metal fluoride-assisted sulfur post-treatment. This method enhanced the uniform distribution of sulfur and selenium (S/Se) as well as energy level alignment that facilitated efficient charge transfer [24]. Thus, efficient defect passivation along with band alignment of the back interface is essential for improving hole extraction. Different to aforementioned organic HTL (P3HT, Spiro-OMeTAD etc.), our recent inorganic HTL report, PbS-EDT (PbS quantum dots capped by ethandithiol (EDT) ligands), obtained a record certified efficiency. The corresponding Sb_2S_3/PbS-EDT interface remians a new challenge to be solved.

Herein, we proposed a strategy to modify the back interface of Sb_2S_3 through $PbCl_2$ post-treatment. Systematic characterization revealed that the hole transfer rate was significantly enhanced and charge recombination was markedly suppressed. These improvements were attributed to the diffusion of Cl ions into the Sb_2S_3 lattice, where they filled sulfur vacancies (V_S) and inhibited the formation of antisite defects (Sb_S). Furthermore, the combined effect of Pb and Cl incorporation facilitated p-type doping at the Sb_2S_3 back interface, which increased conductivity and improved energy level alignment. The synergistic effect of defect passivation and energy level alignment resulted in a significant increase in the fill factor (FF) to 66.02% and achieved a champion PCE of 8.05%.

2 Results and discussion

To evaluate the impact of $PbCl_2$ post-treatment on device performance, we fabricated full-inorganic Sb_2S_3 solar cells based on the FTO/CdS/Sb_2S_3/PbS-EDT/Au structure, as shown in Fig. 1(a), where PbS-EDT serves as the HTL reported in our previous work [25]. The schematic of the $PbCl_2$ post-treatment process is shown in Fig. 1(b). Detailed processing steps are described in the experimental section. For the sake of convenience, samples without post-treatment were labeled as control, while samples with $PbCl_2$ post-treatment are denoted as $PbCl_2$-treated samples in the following discussion. Firstly, the concentration of $PbCl_2$ for post-treatment was investigated as shown in Fig. S1 in the Electronic Supplementary Material (ESM). When the concentration of $PbCl_2$ increased from 10 to 40 mg·mL^{-1}, V_{OC} and FF peaked around 30 mg·mL^{-1}, while the short-circuit current density (J_{SC}) showed little variation. According to concentration optimization, we believe that a higher concentration of $PbCl_2$ solution will result in Pb agglomeration. Thus, the optimal concentration for $PbCl_2$ post-treatment was determined to be 30 mg·mL^{-1}. For the control device, the champion device achieved a PCE of 7.20%, with corresponding V_{OC}, J_{SC}, and FF values of 0.696 V, 17.11 mA·cm^{-2}, and 60.48%, respectively. After $PbCl_2$ post-treatment, the V_{OC} increased to 0.713 V, and the FF was significantly improved to 66.02%. The *J*–*V* curves of the control and champion devices are shown in Fig. 1(c). The statistical distribution of photovoltaic parameters for 30 samples is shown in Fig. 1(d). The specific parameters of devices are summarized in Table S1 in the ESM. Surprisingly, both the V_{OC} and FF were improved by $PbCl_2$ post-treatment, with a particularly notable increase in FF from 59.76% ± 0.61% to 64.33% ± 0.85%. This significant enhancement contributed to a marked PCE improvement from 7.20% to 8.05%.

To further investigate the mechanism of $PbCl_2$ post-treatment, X-ray photoelectron spectroscopy (XPS) was used to analyze the interaction between $PbCl_2$ and the Sb_2S_3 surface, as shown in Fig. S2 in the ESM. Figures 2(a) and 2(b) show the high-resolution XPS spectra of Pb 4f and Cl 2p for the Sb_2S_3 films before and after $PbCl_2$ post-treatment. After $PbCl_2$ treatment, two peaks were observed at 142.5 and 137.6 eV, corresponding to the Pb $4f_{5/2}$ and Pb $4f_{7/2}$ peaks of Pb–S bond, respectively [26]. This indicated successful incorporation of Pb element and interaction with S elements. On the other hand, there were two peaks at binding energies of 201.2 and 197.6 eV, corresponding to the Cl $2p_{1/2}$ and Cl $2p_{3/2}$ orbitals, respectively. This indicated the presence of Cl on the surface of Sb_2S_3 [27]. The high-resolution spectra of the Sb 3d and S 2p orbitals before and after treatment with $PbCl_2$ are shown in Figs. 2(c) and 2(d). For the $PbCl_2$ treated film, two peaks were observed at 538.7 and 529.3 eV, corresponding to the Sb $3d_{3/2}$ and Sb $3d_{5/2}$ peaks (Fig. 2(c)), approximately 0.3 eV shift towards lower binding energies compared to the control film. Additionally, S_{2p}

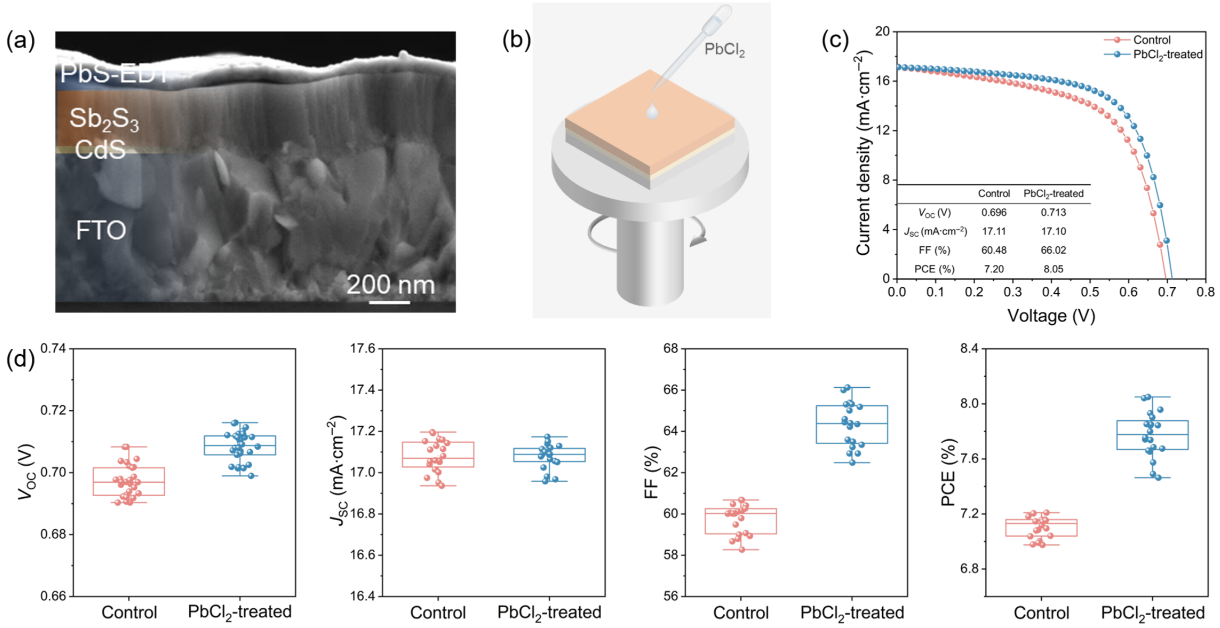

	Control	$PbCl_2$-treated
V_{OC} (V)	0.696	0.713
J_{SC} (mA·cm^{-2})	17.11	17.10
FF (%)	60.48	66.02
PCE (%)	7.20	8.05

Figure 1 (a) A cross-sectional SEM image of the Sb_2S_3 solar cell. (b) The schematic of the $PbCl_2$ post-treatment process. (c) The *J*–*V* curves of the corresponding champion Sb_2S_3 solar cells. (d) Statistical boxplots of V_{OC}, J_{SC}, FF, and PCE.

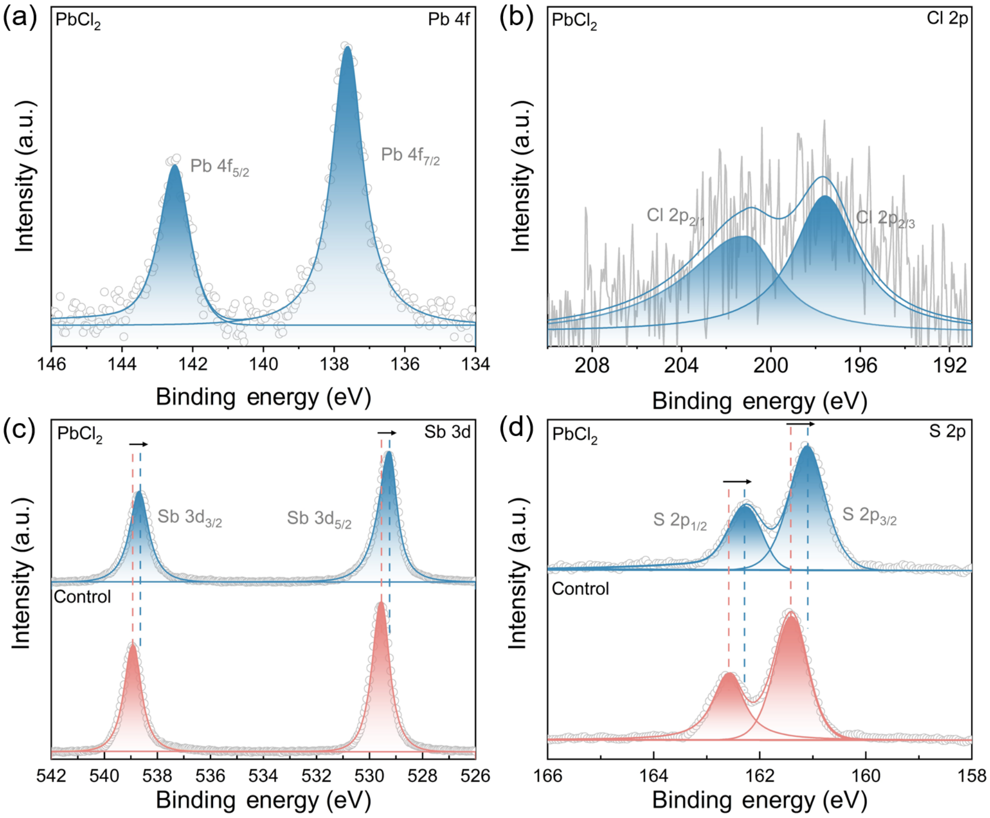

Figure 2 The high-resolution XPS spectra of (a) Pb 4f, (b) Cl 2p, (c) Sb 3d, and (d) S 2p.

signals of the treated film also showed a shift of approximately 0.3 eV towards lower binding energies referring to the control film (Fig. 2(d)). The shift in binding energies for Sb and S elements indicated a change in their binding environment, suggesting that the introduction of Pb and Cl had interacted with Sb_2S_3 [28].

Since XPS measurement can only analyze the surface of the sample around a few nanometers, transmission electron microscopy (TEM) was further employed to analyze the elemental distribution in the bulk phase of the Sb_2S_3 film. Figures 3(a)–3(f) display cross-section TEM images and the corresponding elemental mapping obtained using energy dispersive X-ray spectrometry (EDX) for the $PbCl_2$ post-treatment sample. It can be observed that Pb only enriched at the interface and did not penetrate to the bulk of the Sb_2S_3 (Fig. 3(e)). This was likely due to the relatively large atomic radius of Pb, which made it difficult to diffuse into the bulk of Sb_2S_3. The scanning electron microscopy (SEM) images of the Sb_2S_3 films before and after treatment (Fig. S3 in the ESM) revealed no obvious change in film morphology. X-ray diffraction (XRD) measurements also demonstrated similar spectra (Fig. S4(a) in the ESM). Figure S4(b) in the ESM shows an enlarged view of the main diffraction peaks in 14°–26° range, where a noticeable increase in the intensity of the (020), (120), and (130) diffraction peaks can be clearly observed. And the full width at half maximum (FWHM) values of the (020), (120), and (130) crystal planes decrease from 0.237, 0.187, and 0.192 to 0.229, 0.137, and 0.172, respectively, which indicate that the $PbCl_2$ post-treatment enhances the crystallinity of the Sb_2S_3 film, as shown in Fig. S5 in the ESM. Although there was some enrichment of elemental Cl at the Sb_2S_3 back interface (Fig. 3(f)), the signal of elemental Cl was observed in the bulk phase of the Sb_2S_3 film, which indicated that Cl ions could diffuse into the Sb_2S_3 lattice through $PbCl_2$ post-treatment. Given that the electronegativity of Cl is greater than that of S, stronger interactions between Sb and Cl are expected, which is consistent with the XPS results [21]. The working mechanism of Pb and Cl will be further investigated in the later part.

Since the Pb element only existed at the interface, we further investigated its interfacial modifying effect to HTL. Firstly, contact angle measurements were performed on Sb_2S_3 films before and after $PbCl_2$ treatment using PbS quantum dots solution as the testing liquid as shown in Fig. 4(a). A decrease of contact angle was observed for the $PbCl_2$ post-treatment Sb_2S_3 films, indicating improved wettability with the HTL. It was likely due to the presence of Pb at the back interface, which may form strong chelating with sulfur of HTL [29]. Kelvin probe force microscopy (KPFM) was performed to characterize the surface potential (φ) distribution maps (Fig. 4(b)). After $PbCl_2$ post-treatment, the φ of the Sb_2S_3 film decreased by approximately 30 mV, a lower φ value for the film surface indicated a higher work function and a reduced Fermi level (E_F) [29]. This suggested an increase in the p-type doping concentration at the surface of the Sb_2S_3 film. From the conductive atomic force microscopy (cAFM) measurements shown in Fig. 4(c), it can be observed that the conductivity of the back interface of the Sb_2S_3 film is significantly enhanced after $PbCl_2$ post-treatment. As shown in Fig. 4(d), there is a 0.3 eV valence band offset at the Sb_2S_3/HTL interface. This cliff-like band alignment induces carrier recombination at the interface (Fig. 4(e)). After $PbCl_2$ post-treatment, the valence band maximum (VBM) value of $PbCl_2$ treated Sb_2S_3 had been shifted upward by 0.2 eV at the back interface and the cliff-like band alignment was alleviated (Fig. 4(f)), according to ultraviolet photoelectron spectroscopy (UPS) measurements (Fig. S6 in the ESM). Furthermore, the upward bending of the conduction band effectively repelled the electron

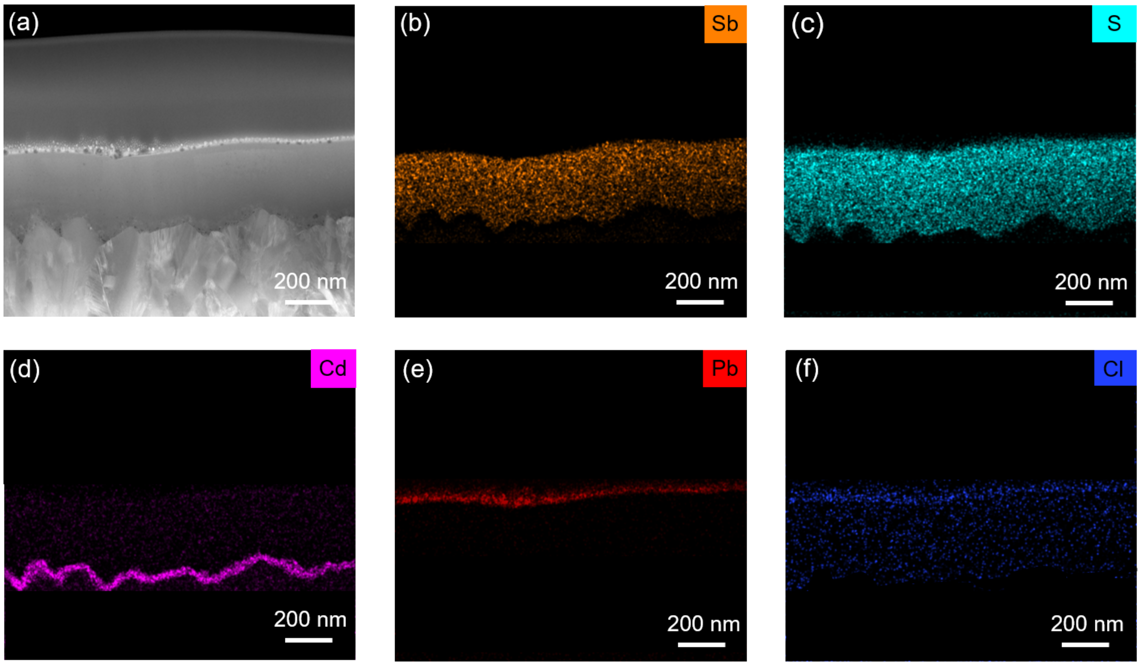

Figure 3 (a) Cross-sectional TEM image of $PbCl_2$ post-treatment Sb_2S_3 samples. (b)–(f) The corresponding element mapping images. All the element distribution is uniform.

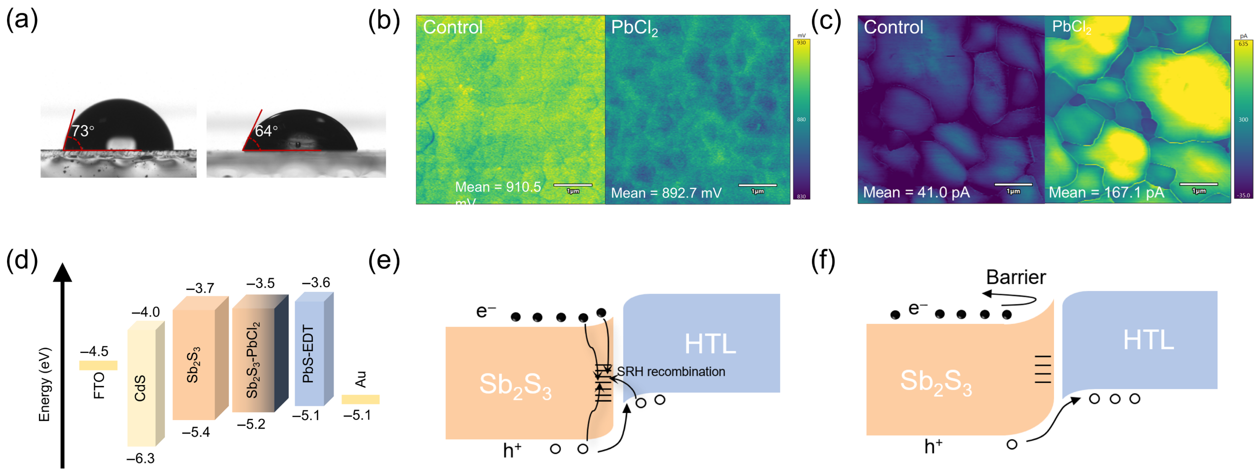

Figure 4 (a) Contact angles of control and $PbCl_2$ post-treatment Sb_2S_3 films using PbS quantum dots solution as the testing liquid. (b) KPFM images. (c) cAFM images. (d) Energy levels of each layer in Sb_2S_3 solar cells except of absorber layers [4]. Energy diagram for (e) the control and (f) $PbCl_2$ post-treatment Sb_2S_3 devices.

diffusion toward the Sb_2S_3/HTL interface and suppressed photocarrier recombination. Based on the above test analysis, the improvement in energy level alignment and conductivity at the back interface significantly enhanced hole extraction efficiency, leading to an increase in FF.

Next, the working mechanism of $PbCl_2$ post-treatment was uncovered for the defect evolution (Fig. 5). V_S defects are one kind of the main defects in Sb_2S_3. And another typical one is Sb_S antisite deep defect, where some Sb ions preferentially fill the V_S instead of Sb_i due to the lower formation energy [30]. After $PbCl_2$ treatment, chlorine (Cl) ions can diffuse into the Sb_2S_3 bulk phase. Due to its higher electronegativity compared to S, Cl forms stronger interactions with Sb comparing with S (Fig. 2(b)), allowing Cl ions to occupy V_S sites, marked by red dashed circles. For Sb_S antisite defects, because of the stronger interaction of Sb–Cl comparing with Sb–Sb_S, Cl incorporation could also suppress the density of Sb_S defects (green dashed circles) [31, 32]. For surface Pb^{2+} effect, previous studies have reported that efficient p-type doping of Sb_2S_3 is quite difficult due to the high concentration of V_S defects and one-dimensional crystal structure, which induce dopant compensation [17, 33]. There is one chance that the rich V_S defects are filled firstly, then p-type dopants can work according to theoretical calculations [17]. In present treatment, assisted by the synergistic effect of chlorine passivation to V_S, Pb elements are proposed to form Pb_{Sb}, leading to efficient p-type doping at the Sb_2S_3 back interface (black dashed circles). Thus, the back mechanism of $PbCl_2$ post-treatment could be summarized as follows. Firstly, Cl atoms passivated V_S and Sb_S defects to suppress the back surface photocarrier recombination. Secondly, Pb enabled effective p-type doping at the Sb_2S_3 interface with the Cl help of V_S removal. Finally, the synergistic effect of Pb and Cl elements matched well with HTL energy level, facilitated hole extraction and enhanced the interface conductivity.

In order to further investigate the effect of $PbCl_2$ post-treatment

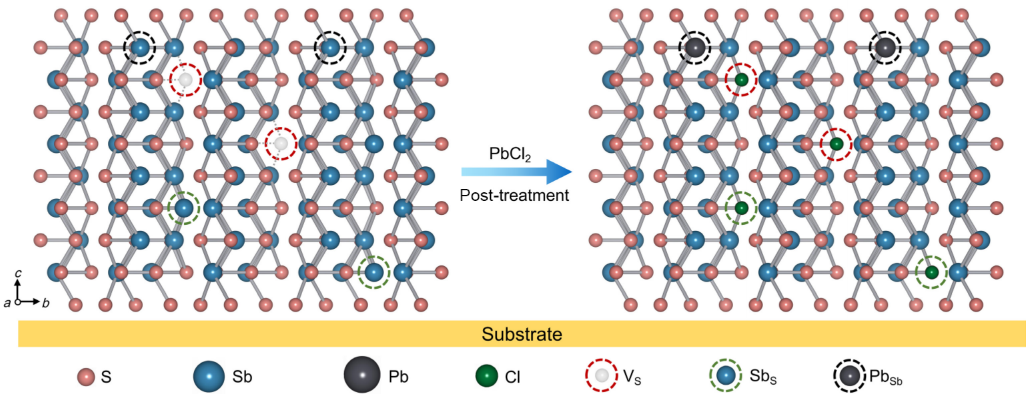

Figure 5 The schematic illustration of the proposed mechanism for PbCl$_2$ post-treatment. Both Pb and Cl elements play vital roles in defect passivation.

on the devices, temperature-dependent *J*–*V* measurements were performed on the control and PbCl$_2$ treated devices as shown in Fig. S7 in the ESM. The *J*–*V* curves of the control device exhibited a kink across the entire temperature range, indicating the presence of a band offset between the Sb$_2$S$_3$ and HTL layers [31, 32]. On the contrary, the device with PbCl$_2$ post-treatment showed kink phenomenon only at temperatures below 200 K, suggesting a reduction in the band offset between Sb$_2$S$_3$ and the HTL. This was consistent with the conclusion drawn from the KPFM test, which indicated an improvement in the energy level alignment at the Sb$_2$S$_3$ back interface.

The temperature-dependent V_{OC} plot was constructed as shown in Fig. 6(a). Extrapolating the V_{OC} versus temperature curve to T = 0 K, the activation energies (E_a) for defects were 1.23 eV for the control device and 1.37 eV for the PbCl$_2$ post-treatment device [33]. These values were lower than the bandgap (E_g), indicating that a significant portion of the interface recombination was present in the Sb$_2$S$_3$ devices [34, 35]. This further verified the importance of interface quality in Sb$_2$S$_3$ devices. On the other hand, the E_a of the PbCl$_2$-treated device was closer to its E_g, indicating the suppressed interface recombination [36].

In order to determine the impact of PbCl$_2$ treatment on the carrier lifetime, transient photovoltage (TPV) test was measured to provide insights into the carrier recombination lifetime of the devices [37]. As shown in Figure 6b, the recombination lifetime (τ) is obtained by fitting with a single-exponential model. For the device with PbCl$_2$ post-treatment, the τ increased significantly from 1.82 to 3.38 μs. This indicated that carrier recombination in the device was significantly suppressed after PbCl$_2$ treatment. Electrochemical impedance spectroscopy (EIS) was further employed to reveal the potential mechanisms of charge transport and recombination in the Sb$_2$S$_3$ solar cells. Figure 6(c) displays the Nyquist plot comprising series resistance (R_s), recombination resistance (R_{rec}), and a constant phase element (CPE). The corresponding values of R_s for control and PbCl$_2$ post-treatment devices were 46.03 and 21.36 Ω·cm^2, and R_{rec} values were 613.98 and 847.32 kΩ·cm^2, respectively. The PbCl$_2$ post-treatment device exhibited a smaller R_s and a larger R_{rec}, which contributed to the

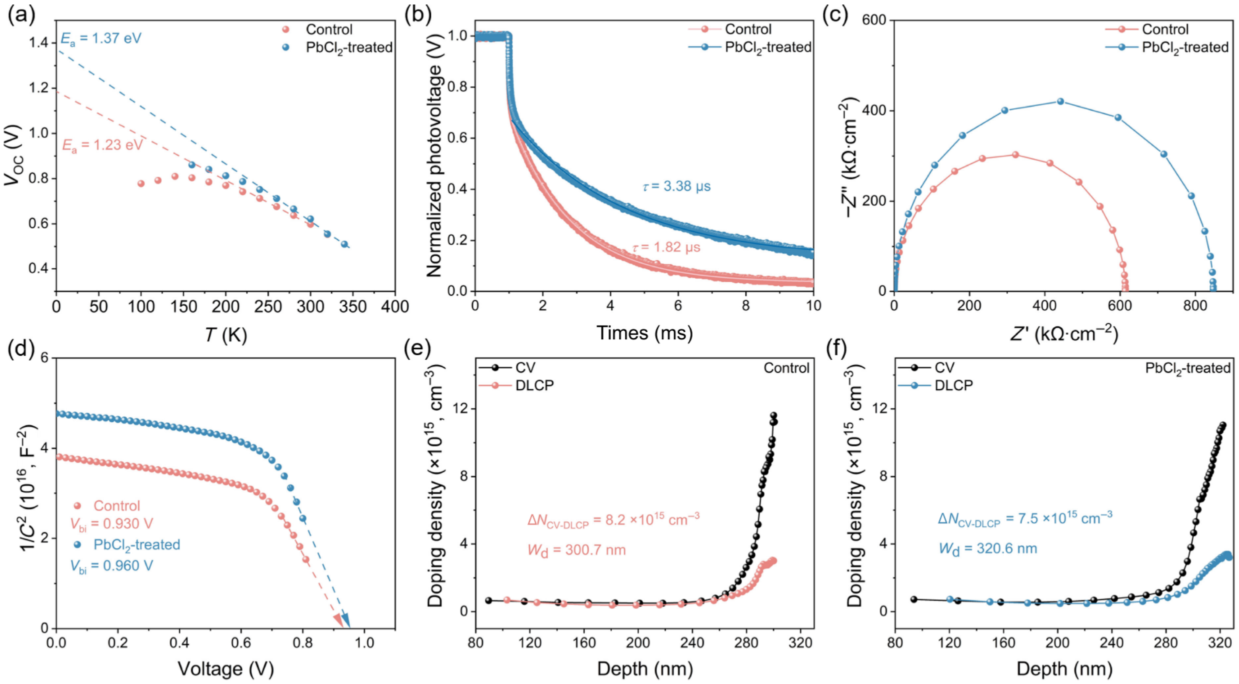

Figure 6 (a) V_{OC} versus temperature curves. (b) Normalized TPV spectra. (c) EIS curves. (d) 1/C^2–V plots of solar cells without and with PbCl$_2$ post-treatment. DLCP spectra of (e) control and (f) PbCl$_2$ post-treatment devices.

improved charge transport efficiency and suppressed carrier recombination.

To further quantitatively analyze the interface defects of Sb_2S_3/HTL, $1/C^2$–V measurements were first conducted as shown in Fig. 6(d). These measurements allowed for the determination of the built-in field (V_{bi}) and the doping concentration of the device. The V_{bi} values of control and $PbCl_2$ post-treatment devices obtained from the X-intercepts of the linear fit were 0.930 and 0.960 V, respectively. The enhanced V_{bi} could favor the separation of photogenerated carriers and improve the carrier transport efficiency [38, 39]. And the doping concentrations were determined to be 4.5×10^{16} and 3.67×10^{16} cm^{-3}, respectively, by analyzing the slope of the $1/C^2$–V curve. The doping density (N_{CV}) obtained from C–V measurements includes the density of free carriers, bulk defect density, and interfacial defect density [39]. While the drive-level capacitance profile (DLCP) measurement is insensitive to interfacial defects, it obains the doping concentration (N_{DLCP}) as the sum of the density of bulk defects and free carriers in the film [40]. Thus, the interfacial defect density $\Delta N_{CV\text{-}DLCP}$ can be calculated by subtracting N_{DLCP} from the N_{CV}. As shown in Figs. 6(e) and 6(f), the interfacial defect density values decrease from 8.2×10^{15} (control) to 7.5×10^{15} cm^{-3} ($PbCl_2$ post-treatment device), and the width values of depletion region (W_d) extend from 300.7 to 320.6 nm. The wider depletion region favored carrier transport by drift rather than diffusion [41].

Carrier dynamics of the films were also analyzed using transient absorption spectroscopy (TAS). Their film samples were FTO/CdS/Sb_2S_3/PbS-EDT and FTO/CdS/Sb_2S_3 ($PbCl_2$ post-treatment)/PbS-EDT, respectively. By adding the HTL layer to enhance the hole transport pathways, we were able to study the effect of the $PbCl_2$ post-treatment. The corresponding two-dimensional (2D) TAS pseudo-color images are shown in Figs. 7(a) and 7(b). In the time-resolved absorption spectra of both samples (Figs. 7(c) and 7(d)), negative peaks were observed at 470–540 and 650–750 nm, corresponding to the ground state bleaching (GSB) peaks of CdS and Sb_2S_3, respectively [7]. For the $PbCl_2$ post-treatment sample, the GSB peak intensity of Sb_2S_3 decreased. This reduction was attributed to the improved hole extraction effect after $PbCl_2$ post-treatment, which allowed a faster recovery of hole concentration to the ground state level [7]. A typical broad-spectrum photoinduced absorption (PIA) peak was also observed in the range of 560–630 nm. This peak was attributed to the photogenerated holes in Sb_2S_3 being trapped at lattice S atoms, forming $S^{\bullet -}$ [39, 42]. In the presence of an HTL, photogenerated holes were rapidly extracted by the HTL. In this case, the decay of the PIA signal in the 560–630 nm range was primarily attributed to hole extraction by HTL. The PIA signal at 570 nm was analyzed by double-exponential fitting as shown in Figs. 7(e) and 7(f). The corresponding results were listed in Table S2 in the ESM. The average hole transfer times were extracted as τ_{av} = 1957 ps for the control and 1637 ps for the $PbCl_2$ post-treatment sample. A shorter transfer time indicated higher hole transport efficiency [43].

The stability of Sb_2S_3 is a key factor in its long-term operation application. To study its stability, we conducted stabilized power output (SPO) tests for control and $PbCl_2$-treated devices. Under conditions of 26 °C and 56% humidity, the efficiency of both types of devices showed almost no decrease in 300 s (Fig. S8(a) in the ESM). We conducted maximum power point tracking for control and $PbCl_2$-treated devices in a nitrogen glove box at 26 °C for 6 months. Results showed that after 6 months, the $PbCl_2$-treated devices maintained over 90% of their initial performance (Fig. S8(b) in the ESM), indicating that the devices exhibited excellent stability.

3 Conclusion

In summary, we developed an efficient $PbCl_2$ post-treatment strategy to modify the interface between Sb_2S_3 and the HTL for Sb_2S_3 solar cells. The interface quality improvement was attributed to two key factors. Firstly, Cl atoms passivated V_S and Sb_S defects to suppress the back surface photocarrier recombination. Secondly, Pb

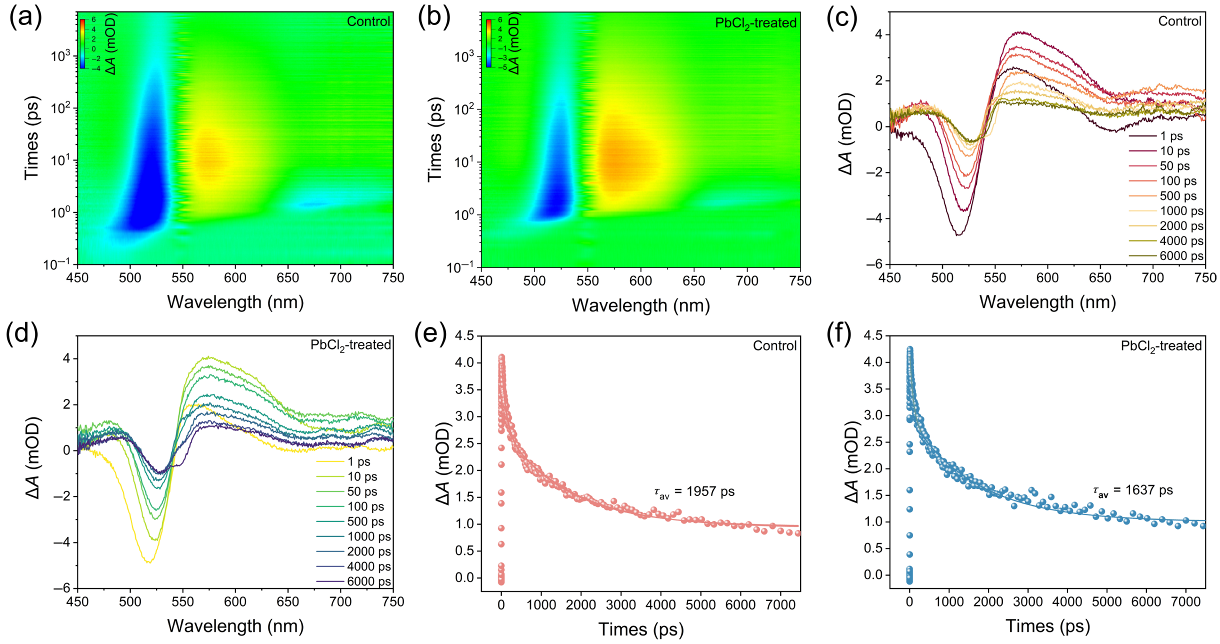

Figure 7 2D TAS pseudo-color images of (a) control and (b) $PbCl_2$ post-treatment Sb_2S_3 film samples. Time-resolved absorption spectra of (c) control and (d) $PbCl_2$ post-treatment samples. Transient kinetic decay (scatter) and fittings according to two-exponential decay function (solid lines) monitored at 570 nm of (e) control and (f) $PbCl_2$ post-treatment Sb_2S_3 samples.

enabled effective p-type doping at the Sb_2S_3 interface with the help of V_S removal. The interfacial defect density values decreased from 8.2×10^{15} to 7.5×10^{15} cm^{-3}, and the average hole transfer times were decreased from 2 to 1.6 ns. The synergistic effect of Cl and Pb incorporation resulted in a significant increase of FF value from 60.48% to 66.02%. Ultimately, we achieved a champion PCE of 8.05% while the control one was 7.2%. This study highlights the critical role of the Sb_2S_3/HTL interface in device performance and provides valuable insights for future research in this area.

4 Experimental section

Preparation of ETL: The substrates were pre-cleaned sequentially with detergent, deionized water, isopropanol, and ethanol using ultrasonic cleaning for 30 min each. They were then dried with a nitrogen stream. The In-doped CdS buffer layer was subsequently deposited using the chemical bath deposition method, and the specifics of the $CdCl_2$ post-treatment followed our previous work [7].

Preparation of Sb_2S_3 absorber and device fabrication: Sb_2S_3 films were deposited using a hydrothermal method, with $KSbC_4H_4O_7{\cdot}0.5H_2O$ and $Na_2S_2O_3{\cdot}5H_2O$ serving as the Sb and S sources. In an 80 mL Teflon tank containing 60 mL of DI water, $KSbC_4H_4O_7{\cdot}0.5H_2O$ (0.4007 g) was added. The mixture was stirred for 10 min before adding selenourea (SU, 0.0045 g) and $Na_2S_2O_3{\cdot}5H_2O$ (1.1912 g), followed by another 10 min of stirring. The substrates were then placed in the Teflon tank with the CdS film facing down. The teflon tank was heated in an oven at 117 °C for 300 min. After the reaction was finished and the teflon tank was cooled to room temperature, the as-grown Sb_2S_3 film was removed and washed with deionized water and blown dry with N_2, and then the as-grown Sb_2S_3 film was treated by spin-coating $PbCl_2$ dimethylformamide solution. The spin-coating speed was 2500 rpm, the acceleration was 1250 rpm/s, and the duration was 20 s. After post-treatment with $PbCl_2$, the as-grown Sb_2S_3 film was annealed in a glove box filled with N_2 at 340 °C for 10 min. The Sb_2S_3 film was annealed at 340 °C on a hot plate, which was set at target temperature in advance according to our previous experience [6]. Then two layers of PbS QDs (1st exciton peak at 880 nm) were treated with EDT ligand (PbS-EDT) acting as the HTL, for specific details, please refer to our previous work on quantum dot synthesis. An 80 nm Au electrode was prepared by thermal evaporation at a deposition rate of approximately 1 $Å{\cdot}s^{-1}$. The final solar cell structure consisted of FTO/CdS/Sb_2S_3/PbS-EDT/Au. The active area of the device was 0.04 cm^2 as defined by the mask.

Characterization: The images of SEM of films were obtained by Gemini SEM 3000-71-12. Crystal structure and phase of Sb_2S_3 thin films characterized by XRD (Philips, X pert pro MRD, Cu Kα radiation). The KPFM and cAFM were measured by atomic force microscopy (Jupiter XR). The cross-section samples of Sb_2S_3 devices were prepared by a focus ion beam system (FIB, Helios 5) and the cross-sectional TEM images of Sb_2S_3 sample were collected by transmission electron microscopy (Tecnai G2 F30). The J–V curves were measured under a simulated AM1.5G (100 $mW{\cdot}cm^{-2}$) illumination from a 450 W xenon lamp (Oriel, Model 9119, Newport) combined with a source meter (Keithley 2400) at 25 °C in the air. And C–V measurements were conducted using an Agilent 4200A at room temperature with a frequency of 10 kHz and alternating current (AC) amplitude of 20 mV. The direct current (DC) bias voltage was swept from −1.0 to 0.8 V. DLCP measurements were performed with the AC variant amplitude (20–200 mV) and the DC bias from −0.1 to 0.8 V. TPV and TPC were measured by a system consisting of 530 nm monochromatic light, function generator, and oscilloscope The minority carrier lifetime of the films was characterized using transient absorption spectroscopy (TAS) with a Spirit 1040-8-SHG system. The testing setup included a commercial femtosecond laser (Model: Legend Elite, Coherent) with a pump wavelength of 550 nm.

Electronic Supplementary Material: Supplementary material (characterizations of films and devices, Figs. S1–S8, and Tables S1 and S2) is available in the online version of this article at https://doi.org/10.26599/NR.2025.94908031.

Data availability

All data needed to support the conclusions in the paper are presented in the manuscript and the Electronic Supplementary Material. Additional data related to this paper may be requested from the corresponding author upon request.

Acknowledgements

This work was supported by the National Natural Science Foundation of China (No. 62374065), the Interdisciplinary Research Promotion of HUST (No. 2023JCYJ040), Project for Building a Science and Technology Innovation Center Facing South Asia and Southeast Asia (No. 202403AP140015), and the Innovation Project of Optics Valley Laboratory (No. OVL2024BB017). The authors thank Testing Center of HUST and the Center for Nanoscale Characterization & Devices (CNCD), WNLO-HUST for facility access.

Declaration of competing interest

The authors declare that they have no known competing financial interests or personal relationships that could have appeared to influence the work reported in this paper.

Author contribution statement

G. H. S., R. H. G., and H. S. S.: Data curation, validation, writing manuscript, experimental design. S. W. C., A. K., and T. J. M.: Experimental design, validation. S. A., M. Y. L., and H.-Y. H.: Project administration, experimental design. J. T. and H. S. S.: Project administration, funding acquisition. All the authors have approved the final manuscript.

Use of AI statement

None.

References

[1] Zhu, M. F.; Qin, L. N.; Xia, Y. R.; Mao, L. Y.; Zhao, P. Y.; Zhao, C.; Hu, Y.; Hong, D. C.; Tian, Y. X.; Tie, Z. X. et al. Indium-doped $CsPbI_{2.5}Br_{0.5}$ with a tunable band structure and improved crystallinity for thermo-stable all-inorganic perovskite solar cells. *ACS Appl. Energy Mater.* **2023**, *6*, 8237–8244.

[2] Zhu, M. F.; Qin, L. N.; Xia, Y. R.; Liang, J. C.; Wang, Y. D.; Hong, D. C.; Tian, Y. X.; Tie, Z. X.; Jin, Z. Antimony doped $CsPbI_2Br$ for

high-stability all-inorganic perovskite solar cells. *Nano Res.* **2024**, *17*, 1508–1515.

[3] Yu, W. J.; Sun, X. R.; Xiao, M.; Hou, T.; Liu, X.; Zheng, B. L.; Yu, H.; Zhang, M.; Huang, Y. L.; Hao, X. J. Recent advances on interface engineering of perovskite solar cells. *Nano Res.* **2022**, *15*, 85–103.

[4] Shah, U. A.; Chen, S. W.; Khalaf, G. M. G.; Jin, Z. X.; Song, H. S. Wide bandgap Sb_2S_3 solar cells. *Adv. Funct. Mater.* **2021**, *31*, 2100265.

[5] Kondrotas, R.; Chen, C.; Tang, J. Sb_2S_3 solar cells. *Joule* **2018**, *2*, 857–878.

[6] Shen, G. H.; Ke, A.; Chen, S. W.; Ma, T. J.; Ali, S.; Li, M. Y.; Hsu, H. Y.; Chen, C.; Yang, P. Z.; Song, H. S. et al. Strong chelating additive and modified electron transport layer for 8.26%-efficient Sb_2S_3 solar cells. *Adv. Energy Mater.* **2025**, *15*, 2406051.

[7] Chen, S. W.; Li, M. Y.; Zhu, Y. C.; Cai, X. Q.; Xiao, F.; Ma, T. J.; Yang, J.; Shen, G. H.; Ke, A.; Lu, Y. et al. A codoping strategy for efficient planar heterojunction Sb_2S_3 solar cells. *Adv. Energy Mater.* **2022**, *12*, 2202897.

[8] Wang, S. Y.; Zhao, Y. Q.; Che, B.; Li, C.; Chen, X. L.; Tang, R. F.; Gong, J. B.; Wang, X. M.; Chen, G. L.; Chen, T. et al. A novel multi-sulfur source collaborative chemical bath deposition technology enables 8%-efficiency Sb_2S_3 planar solar cells. *Adv. Mater.* **2022**, *34*, 2206242.

[9] Nicolás-Marín, M. M.; Vigil-Galán, O.; Ayala-Mato, F.; Courel, M. Analysis of hole transport layer and electron transport layer materials in the efficiency improvement of $Sb_2(Se_{1-x}S_x)_3$ solar cell. *Phys. Status Solidi (B)* **2023**, *260*, 2200342.

[10] Ayala-Mató, F.; Vigil-Galán, O.; Nicolás-Marín, M. M.; Courel, M. Study of loss mechanisms on $Sb_2(S_{1-x}Se_x)_3$ solar cell with n–i–p structure: Toward an efficiency promotion. *Appl. Phys. Lett.* **2021**, *118*, 073903.

[11] Xu, Y. F.; Chen, W. Y.; Ding, X. H.; Pan, X.; Hu, L. H.; Yang, S. F.; Zhu, J.; Dai, S. Y. An ultrathin SiO_2 blocking layer to suppress interfacial recombination for efficient Sb_2S_3-sensitized solar cells. *Inorg. Chem. Front.* **2018**, *5*, 1370–1377.

[12] Han, J.; Pu, X. Y.; Zhou, H.; Cao, Q.; Wang, S. J.; He, Z. W.; Gao, B. Y.; Li, T. T.; Zhao, J. S.; Li, X. H. Synergistic effect through the introduction of inorganic zinc halides at the interface of TiO_2 and Sb_2S_3 for high-performance Sb_2S_3 planar thin-film solar cells. *ACS Appl. Mater. Interfaces* **2020**, *12*, 44297–44306.

[13] Li, J. M.; Zhao, Y. Q.; Li, C.; Wang, S. Y.; Chen, X. L.; Gong, J. B.; Wang, X. M.; Xiao, X. D. Hydrazine hydrate-induced surface modification of CdS electron transport layer enables 10.30%-efficient $Sb_2(S, Se)_3$ planar solar cells. *Adv. Sci.* **2022**, *9*, 2202356.

[14] Zhang, T. Y.; Yang, Y. S.; Dong, J. J.; Shen, B. Z.; Zhang, J. L.; Zhang, S.; Zhang, H.; Lu, M. L.; Jiang, S.; Qiu, J. H. et al. Regulation of the charge carrier dynamics in antimony selenide thin-film solar cells based on the effective diffusion of ions at the heterojunction interface. *Adv. Funct. Mater.* **2025**, *35*, 2417868.

[15] Liang, X. Y.; Wang, X. H.; Chang, Q. W.; Yang, B. X.; Dang, W.; Zhang, Z.; Guo, Y. N.; Yang, L.; Li, Z. Q. Reduction of bulk and interface defects via photo-annealing treatment for high-efficiency antimony selenide solar cells. *Energy Environ. Sci.* **2024**, *17*, 9499–9508.

[16] Tsujimoto, K.; Nguyen, D. C.; Ito, S.; Nishino, H.; Matsuyoshi, H.; Konno, A.; Kumara, G. R. A.; Tennakone, K. TiO_2 surface treatment effects by Mg^{2+}, Ba^{2+}, and Al^{3+} on Sb_2S_3 extremely thin absorber solar cells. *J. Phys. Chem. C* **2012**, *116*, 13465–13471.

[17] Cai, Z. H.; Dai, C. M.; Chen, S. Y. Intrinsic defect limit to the electrical conductivity and a two-step p-type doping strategy for overcoming the efficiency bottleneck of Sb_2S_3-based solar cells. *Solar RRL* **2020**, *4*, 1900503.

[18] Guo, L. P.; Zhang, B. Y.; Li, S.; Zhang, Q.; Buettner, M.; Li, L.; Qian, X. F.; Yan, F. Scalable and efficient Sb_2S_3 thin-film solar cells fabricated by close space sublimation. *APL Materials* **2019**, *7*, 041105.

[19] Li, J. S.; Xiong, L. B.; Hu, X. Z.; Liang, J. W.; Chen, C.; Ye, F. H.; Li, J.; Liu, Y. J.; Shao, W. L.; Wang, T.; et al. Manipulating the morphology of CdS/Sb_2S_3 heterojunction using a Mg-doped tin oxide buffer layer for highly efficient solar cells. *J. Energy Chem.* **2022**, *66*, 374–381.

[20] Nicolás-Marín, M. M.; González-Castillo, J. R.; Vigil-Galán, O.; Courel, M. The state of the art of $Sb_2(S, Se)_3$ thin film solar cells: Current progress and future prospect. *J. Phys. D: Appl. Phys.* **2022**, *55*, 303001.

[21] Choi, Y. C.; Lee, D. U.; Noh, J. H.; Kim, E. K.; Seok, S. I. Highly improved Sb_2S_3 sensitized-inorganic-organic heterojunction solar cells and quantification of traps by deep-level transient spectroscopy. *Adv. Funct. Mater.* **2014**, *24*, 3587–3592.

[22] Yuan, S. J.; Deng, H.; Yang, X. K.; Hu, C.; Khan, J.; Ye, W. N.; Tang, J.; Song, H. S. Postsurface selenization for high performance Sb_2S_3 planar thin film solar cells. *ACS Photonics* **2017**, *4*, 2862–2870.

[23] Xiao, F.; Chen, S. W.; You, F. G.; Ma, T. J.; Chen, C.; Hsu, H. Y.; Song, H. S.; Tang, J. Confined-space selenium-assisted tellurization posttreatment strategy for efficient full-inorganic Sb_2S_3 thin-film solar cells. *Energy Tech.* **2023**, *11*, 2201315.

[24] Zhao, Y. Q.; Wang, S. Y.; Jiang, C. H.; Li, C.; Xiao, P.; Tang, R. F.; Gong, J. B.; Chen, G. L.; Chen, T.; Li, J. M. et al. Regulating energy band alignment via alkaline metal fluoride assisted solution post-treatment enabling $Sb_2(S, Se)_3$ solar cells with 10.7% efficiency. *Adv. Energy Mater.* **2022**, *12*, 2103015.

[25] Chen, S. W.; Zhao, X. Z.; Shen, G. H.; Ke, A.; Liu, B. H.; Hsu, H. Y.; Chen, C.; Yang, P. Z.; Tang, J.; Song, H. S. All-inorganic Sb_2S_3-based two-terminal tandem solar cells enable over 10.9% efficiency employing a concise interconnection layer. *J. Mater. Chem. A* **2024**, *12*, 18148–18156.

[26] Zheng, X. L.; Lei, H. W.; Yang, G.; Ke, W. J.; Chen, Z. L.; Chen, C.; Ma, J. J.; Guo, Q. B.; Yao, F.; Zhang, Q. et al. Enhancing efficiency and stability of perovskite solar cells via a high mobility p-type PbS buffer layer. *Nano Energy* **2017**, *38*, 1–11.

[27] Han, J.; Wang, S. J.; Yang, J. B.; Guo, S. H.; Cao, Q.; Tang, H. J.; Pu, X. Y.; Gao, B. Y.; Li, X. H. Solution-processed Sb_2S_3 planar thin film solar cells with a conversion efficiency of 6.9% at an open circuit voltage of 0.7 V achieved via surface passivation by a $SbCl_3$ interface layer. *ACS Appl. Mater. Interfaces* **2020**, *12*, 4970–4979.

[28] Wu, F. Y.; Zhao, Y. Q.; Yao, L. Q.; Li, H.; Huang, Z. P.; Lin, L. M.; Ma, Y. P.; Chen, S. Y.; Li, J. M.; Chen, G. L. Manipulating back contact enables over 8%-efficient carbon-based $Sb_2(S, Se)_3$ solar cells. *Chem. Eng. J.* **2022**, *440*, 135872.

[29] Enevoldsen, G. H.; Glatzel, T.; Christensen, M. C.; Lauritsen, J. V.; Besenbacher, F. Atomic scale Kelvin probe force microscopy studies of the surface potential variations on the TiO_2(110) surface. *Phys. Rev. Lett.* **2008**, *100*, 236104.

[30] Cai, Z. H.; Chen, S. Y. Extrinsic dopants in quasi-one-dimensional photovoltaic semiconductor Sb_2S_3: A first-principles study. *J. Appl. Phys.* **2020**, *127*, 183101.

[31] Kim, S.; Rana, T. R.; Kim, J.; Son, D. H.; Yang, K. J.; Kang, J. K.; Kim, D. H. Limiting effects of conduction band offset and defect states on high efficiency CZTSSe solar cell. *Nano Energy* **2018**, *45*, 75–83.

[32] Khatri, I.; Lin, T. Y.; Yashiro, T.; Sugiyama, M. Temperature-dependent current-voltage and admittance spectroscopy analysis on cesium-treated Cu $(In_{1-x}, Ga_x)Se_2$ solar cell before and after heat-light soaking and subsequent heat-soaking treatments. *Prog. Photovolt: Res. Appl.* **2020**, *28*, 1158–1166.

[33] Nadenau, V.; Rau, U.; Jasenek, A.; Schock, H. W. Electronic

properties of $CuGaSe_2$-based heterojunction solar cells. Part I. Transport analysis. *J. Appl. Phys.* **2000**, *87*, 584–593.

[34] Park, G. S.; Chu, V. B.; Kim, B. W.; Kim, D. W.; Oh, H. S.; Hwang, Y. J.; Min, B. K. Achieving 14.4% alcohol-based solution-processed Cu(In, Ga)(S, $Se)_2$ thin film solar cell through interface engineering. *ACS Appl. Mater. Interfaces* **2018**, *10*, 9894–9899.

[35] Yang, K. J.; Sim, J. H.; Jeon, B.; Son, D. H.; Kim, D. H.; Sung, S. J.; Hwang, D. K.; Song, S.; Khadka, D. B.; Kim, J. et al. Effects of Na and MoS_2 on Cu_2ZnSnS_4 thin-film solar cell. *Prog. Photovolt: Res. Appl.* **2015**, *23*, 862–873.

[36] Cao, L.; Wang, L. J.; Zhou, Z. J.; Zhou, T. X.; Li, R.; Zhang, H.; Wang, Z. T.; Wu, S. X.; Najar, A.; Tian, Q. W. et al. Modifying surface termination by bidentate chelating strategy enables 13.77% efficient kesterite solar cells. *Adv. Mater.* **2024**, *36*, 2311918.

[37] Gong, Y. C.; Zhu, Q.; Li, B. Y.; Wang, S. S.; Duan, B. W.; Lou, L. C.; Xiang, C. X.; Jedlicka, E.; Giridharagopal, R.; Zhou, Y. G. et al. Elemental de-mixing-induced epitaxial kesterite/CdS interface enabling 13%-efficiency kesterite solar cells. *Nat. Energy* **2022**, *7*, 966–977.

[38] Deng, H.; Zeng, Y. Y.; Ishaq, M.; Yuan, S. J.; Zhang, H.; Yang, X. K.; Hou, M. M.; Farooq, U.; Huang, J. L.; Sun, K. W. et al. Quasiepitaxy strategy for efficient full-inorganic Sb_2S_3 solar cells. *Adv. Funct. Mater.* **2019**, *29*, 1901720.

[39] Wang, C.; Lu, S. C.; Li, S.; Wang, S. Y.; Lin, X. T.; Zhang, J.; Kondrotas, R.; Li, K. H.; Chen, C.; Tang, J. Efficiency improvement of flexible Sb_2Se_3 solar cells with non-toxic buffer layer via interface engineering. *Nano Energy* **2020**, *71*, 104577.

[40] Heath, J. T.; Cohen, J. D.; Shafarman, W. N. Bulk and metastable defects in $CuIn_{1-x}Ga_xSe_2$ thin films using drive-level capacitance profiling. *J. Appl. Phys.* **2004**, *95*, 1000–1010.

[41] Ohnesorge, B.; Weigand, R.; Bacher, G.; Forchel, A.; Riedl, W.; Karg, F. H. Minority-carrier lifetime and efficiency of Cu(In, $Ga)Se_2$ solar cells. *Appl. Phys. Lett.* **1998**, *73*, 1224–1226.

[42] Christians, J. A.; Kamat, P. V. Trap and transfer. Two-step hole injection across the Sb_2S_3/CuSCN interface in solid-state solar cells. *ACS Nano* **2013**, *7*, 7967–7974.

[43] Lian, W. T.; Jiang, C. H.; Yin, Y. W.; Tang, R. F.; Li, G.; Zhang, L. J.; Che, B.; Chen, T. Revealing composition and structure dependent deep-level defect in antimony trisulfide photovoltaics. *Nat. Commun.* **2021**, *12*, 3260.